# Design of architected materials for thermoelastic macrostructures using level set method

Lei Li<sup>1</sup>, Zongliang Du<sup>1</sup> and H. Alicia Kim<sup>1,2</sup>

#### **Abstract**

In this study, a level set topology optimization method is introduced and used to design optimized periodic architected materials for the maximum macrostructural stiffness considering thermoelasticity. The design variables are defined at the microscopic scale and updated by minimizing the total structural compliance induced by mechanical and thermal expansion loads at the macroscopic scale. The two scales are coupled by the effective elasticity tensor calculated through the homogenization theory. A decomposition method is constructed to formulate several sub-problems from the original optimization problem thereby this otherwise computationally expensive problem can be efficiently solved, especially when the number of material subdomains is large. The proposed method is demonstrated through several numerical examples. It is shown that a macrostructural geometry and boundary conditions have a significant impact on the optimized material designs when thermoelastic effects are considered. Porous material with well-designed microstructure is preferred over solid material when a thermal load is non-zero. Moreover, when a larger number of material microstructures is allowed in optimization, the overall performance is improved due to the expanded design space.

**Keywords**: Architected porous material; Topology optimization; Level set method; Multiscale; Homogenization; Thermoelasticity.

<sup>&</sup>lt;sup>1</sup> Structural Engineering Department, University of California, San Diego, 9500 Gilman Drive, San Diego, CA 92093, USA (Corresponding Author: Lei Li, email: lel008@eng.ucsd.edu)

<sup>&</sup>lt;sup>2</sup> Cardiff School of Engineering, Cardiff University, The Queen's Buildings, 14-17 The Parade, Cardiff, CF24 3AA, United Kingdom

#### 1. Introduction

Cellular materials composed of periodically repeated porous unit cells with special microscale architectures have shown a significant potential in various engineering applications [1,2] because of their tailorable properties, such as high stiffness to density ratio, high permeability, low thermal conductivity and other exotic properties that are usually unattained at the bulk scale [3,4]. The properties of these architected materials not only rely on the basic material constituents, but also strongly depend on the spatial arrangement of void and solids – that is, the configuration of the cellular microarchitecture. Thanks to the recently emerging additive manufacturing (AM) technologies with the improving feature controls at small scales, great opportunities are opened up to fabricate architected materials with unprecedentedly complex geometries and features [5,6]. As a result, the purposeful design of materials with tailored microstructures to achieve desired properties for specific applications at macroscale is attracting ever-increasing attention.

Before AM became an active research field, design of architected materials using topology optimization has already flourished, and the first attempt was made by Sigmund [7], in which the homogenized material effective properties were optimized to the desired values. Based on the idea of inverse homogenization proposed in [7], topology optimization has been applied for architected material designs aiming to (a) achieve extremal material properties, such as maximum bulk or shear moduli [8–12], minimum negative Poisson's ratio [10], extremal thermal expansion [13], maximum band-gaps [14] and energy dissipation capacity [15]; or (b) tailor material properties to the target values, e.g. effective Young's moduli [16], Poisson's ratio [17–19]; or (c) realize multifunctionality, such as simultaneous heat and electricity transportation [20], permeability and stiffness [21], conductivity and stiffness [22], and viscoelastic damping and stiffness maximizations

[23]. Readers are referred to [24,25] and the references therein for more comprehensive reviews on this topic.

Topology optimization is considered ideal for AM design due to its free-form formulation, expanded design space, and flexibility [26]. The first AM of topologically optimized material can be traced back to Sigmund [27], in which a microstructure with maximum piezoelectric charge coefficient was fabricated by stereolithography. Later on, Hollister [28] used selective laser sintering to build the optimized lattice scaffold in tissue engineering. With the advances of AM, more topology-optimized architected materials have been realized by various processing techniques in recent years. For example, negative Poisson's ratio by metal electron beam melting [29], nylon selective laser melting [30], and silicone direct ink writing [31]; tunable thermal expansion by multi-material photopolymer AM [32,33]; stiffness by Ti-Al6-V4 alloy selective laser melting [36].

Despite the success of the abovementioned topology optimization studies in architected material designs, it should be noted that although the material microstructures are optimized to achieve the extremal or desirable material properties, they are not necessarily efficient or optimal to be used in their composing macrostructure since the macroscopic performance was absent from the material design process in these studies. It is usually unknown what the desired material properties should be to attain the best macroscopic functional performance when used in a structure, not to mention that the macrostructural geometry and boundary conditions are varied in practical use and can significantly affect the optimized material design [37].

To address this deficiency of decoupled material design at only microscale, a hierarchical method to optimize material microstructure and its macrostructure simultaneously was proposed by Rodrigues et al. [38] and Coelho et al. [39] using one unified volume constraint. Later on, Liu

et al. [40] proposed a porous anisotropic material with penalization (PAMP) method for concurrent material and structural design with a single microstructural pattern and two separate volume constraints for both scales. Xia and Breitkopf [41] used the FE<sup>2</sup> approach for a nonlinear multiscale analysis to closely couple microstructural properties to the macroscopic strain field at each optimization iteration, and optimized the designs at both macro and microscale using separate volume constraints. These multiscale design studies either considered uniform or a few [40,42] material microstructures which may not fully explore the design space, or the element-wise material microstructures [39,41], which may be numerically expensive, especially when the number macroelements is large. Sivapuram et al. [43] introduced a generalized problem formulation to simultaneously design structure and any number of material microstructures with arbitrary number or type of constraints. In this formulation, the integrated multiscale optimization problem is decomposed into one macroscale optimization and multiple material microscale optimizations, which then can be efficiently solved by distributed computing. Similar decomposition ideas were adopted in more recent multiscale design studies using parameterized level set method [44,45]. Based on these approaches, various multiscale topology optimization was studied for both linear [46-52] and nonlinear [53–55] material properties.

It should be noted that a majority of the studies on multiscale topology optimization focused on the problems only with mechanical loads. However, in aerospace engineering and advance manufacturing, many structures are subjected to both mechanical and thermal loads simultaneously, such as the thermal protection system of a space shuttle, supporting structures for combustion of jet engines and additively manufactured parts with repeated material heating and cooling. Therefore, how to design optimum architected material for light weight, high thermal stiffness and superior thermal-mechanical properties for these applications has become an active research topic.

With the consideration of thermoelasticity, several topology optimization studies were conducted [56–60] to design structures at macroscale, and it was found that the thermal loads had a big impact on the optimized design and the volume fraction constraint can be inactive when the thermoelastic effect becomes prominent. Coupling the macroscopic thermal elastic properties with the microscopic material distribution, Deng et al. [61] and Yan et al. [62] recently showed that under both mechanical and thermal loads, structures composed of porous materials with well-designed microstructures can substantially enhance the structural stiffness. In these studies, however, only single material microstructure was considered in the optimization with limited macrostructural geometries, which might not have explored the full potential of the architected material design for thermoelastic effects.

In this study, a design method for architected materials considering thermoelasticity is proposed based on the multiscale level set topology optimization framework introduced by Sivapuram et al. [43]. The optimization problem is formulated in such a way that the design variables are optimized at microscale by maximizing total structural stiffness at macroscale under the specified mechanical and thermal loading. The homogenization method is used to compute the material effective properties that bridge the two scales. A decomposition approach is employed to efficiently solve for multiple materials at various macroscopic regions simultaneously in a distributed but coupled manner. Finally, numerical examples are presented to discover the new metamaterial for thermoelasticity. The remainder of this paper is laid out as follows: Section 2 gives the problem formulation for material design with thermoelasticity. Section 3 discusses the multiscale level set topology optimization for solving the problem in Section 2 along with the sensitivity analysis. Section 4 presents a number of optimized microstructure topologies obtained using the proposed approach with the corresponding analyses, followed by the conclusions in Section 5.

# 2. Optimization problem formulation with thermoelasticity

A schematic illustration of the architected material design for a macrostructure is shown in Figure 1, where the macrostructural domain  $\Omega \in \mathbb{R}^d$  (d=2 or 3) is composed of N subdomains ( $\Omega = \bigcup_{I=1}^N \Omega_I$  with N=2 in this figure). Each subdomain has a unique underlying material architecture represented by the periodically repeated unit cell  $Y_I$  with microstructure pattern  $\Omega_{Y_I}$ . The boundary of the macrostructure ( $\Gamma = \partial \Omega$ ) is partitioned into two disjoint segments such that  $\Gamma = \Gamma_u \cup \Gamma_t$  and  $\Gamma_u \cap \Gamma_t = \emptyset$ . The macroscopic domain  $\Omega$  is subjected to body forces  $\boldsymbol{b}$  and temperature change  $\Delta T$ , the surface tractions  $\bar{\boldsymbol{t}}$  are imposed on  $\Gamma_t$  while the displacements are fixed on  $\Gamma_u$ . The boundary value problem for the thermoelastic structure is given as

$$\begin{cases}
\nabla \cdot \boldsymbol{\sigma} + \boldsymbol{b} = \boldsymbol{0} & \text{in } \Omega \\
\boldsymbol{\sigma} \cdot \boldsymbol{n} = \bar{\boldsymbol{t}} & \text{on } \Gamma_t \\
\boldsymbol{u} = \boldsymbol{0} & \text{on } \Gamma_u
\end{cases} \tag{1}$$

where u is the macroscale displacement field and n is the outward normal to the structural boundary,  $\sigma$  denotes the stress tensor which reads

$$\boldsymbol{\sigma} = \mathbb{D}^H : (\boldsymbol{\varepsilon}(\boldsymbol{u}) - \boldsymbol{\varepsilon}^t) \tag{2}$$

where  $\boldsymbol{\varepsilon}(\boldsymbol{u}) = \nabla^s \boldsymbol{u}$  is the strain tensor with  $\nabla^s \boldsymbol{u}$  denoting the symmetric gradient operator,  $\boldsymbol{\varepsilon}^t$  is the thermal strain defined as  $\boldsymbol{\varepsilon}^t = \alpha_T^H \Delta T \boldsymbol{\varepsilon}^0$  for plane stress case where  $\alpha_T^H$  is the effective thermal expansion coefficient,  $\varepsilon_{ij}^0 = \delta_{ij}$  with i,j=1,2 for 2D case and  $\Delta T = T - T_{ref}$  is the uniform temperature change in the structure with respect to the reference temperature  $T_{ref} = 0$ ,  $\mathbb{D}^H$  is the effective elasticity tensor that correlates the macroscale and the microscale.

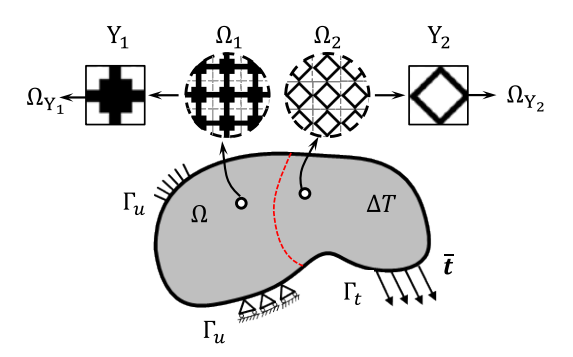


Figure 1. A macrostructure composed of architected materials.

The weak form of Eq. (1) can be expressed as

$$a(\boldsymbol{u}, \boldsymbol{v}) = \bar{a}(\Delta T, \boldsymbol{v}) + \ell(\boldsymbol{v}), \ \forall \boldsymbol{v} \in U_{ad}$$
 (3)

where v is the macroscale virtual displacement that satisfies the kinematically admissible displacement  $U_{ad} = \{v \in H^1(\Omega) \mid v = 0 \text{ on } \Gamma_u\}$  and

$$a(\boldsymbol{u}, \boldsymbol{v}) = \int_{\cup_{I=1}^{N} \Omega_{I}} \boldsymbol{\varepsilon}(\boldsymbol{u}) : \mathbb{D}_{I}^{H} : \boldsymbol{\varepsilon}(\boldsymbol{v}) \ d\Omega$$

$$\bar{a}(\Delta T, \boldsymbol{v}) = \int_{\cup_{I=1}^{N} \Omega_{I}} \boldsymbol{\varepsilon}^{t} : \mathbb{D}_{I}^{H} : \boldsymbol{\varepsilon}(\boldsymbol{v}) \ d\Omega = \int_{\cup_{I=1}^{N} \Omega_{I}} \alpha_{T}^{H} \Delta T \boldsymbol{\varepsilon}^{0} : \mathbb{D}_{I}^{H} : \boldsymbol{\varepsilon}(\boldsymbol{v}) \ d\Omega$$

$$\ell(\boldsymbol{v}) = \int_{\cup_{I=1}^{N} \Omega_{I}} \boldsymbol{b} \cdot \boldsymbol{v} \ d\Omega + \int_{\Gamma_{t}} \bar{\boldsymbol{t}} \cdot \boldsymbol{v} \ d\Gamma$$

$$(4)$$

By assuming that the material unit cell is sufficiently smaller than the macrostructure,  $\mathbb{D}_{I}^{H}$  for unit cell  $Y_{I}$  can be calculated using the asymptotic homogenization theory [63]

$$D_{I,ijkl}^{H} = \frac{1}{|Y_{I}|} \int_{Y_{I}} D_{pqrs} \left( \bar{\varepsilon}_{pq}^{(ij)} - \varepsilon_{pq}^{*(ij)} \right) \left( \bar{\varepsilon}_{rs}^{(kl)} - \varepsilon_{rs}^{*(kl)} \right) dY, \quad (i,j,k,l = 1,2,...,d)$$
 (5)

where  $D_{I,ijkl}^H$  and  $D_{pqrs}$  are the components of the homogenized elasticity tensor  $\mathbb{D}_I^H$  and the base material elasticity tensor  $\mathbb{D}$ , respectively,  $\bar{\varepsilon}^{(ij)}$  is the unit test strain tensor and  $\varepsilon^{*(ij)}$  is the characteristic strain tensor with Y-periodicity that can be determined by solving the canonical equations in the unit cell as

$$\int_{Y_{l}} D_{pqrs} \bar{\varepsilon}_{pq}^{(ij)} \varepsilon_{rs} (\boldsymbol{v}^{(kl)}) dY = \int_{Y_{l}} D_{pqrs} \varepsilon_{pq}^{*} (\boldsymbol{\chi}^{(ij)}) \varepsilon_{rs} (\boldsymbol{v}^{(kl)}) dY, \quad \forall \boldsymbol{v}^{(kl)} \in U_{\boldsymbol{\chi}}$$
 (6)

where  $\chi$  is the characteristic displacement fields in the unit cell and v is the virtual displacement field satisfying the kinematically admissible displacement space  $U_{\chi} = \{v \mid v \text{ is Y - periodic}\}$ .

It has been mathematically proven that for porous material with a single base material,  $\alpha_T^H = \alpha_T$ , where  $\alpha_T$  is the thermal expansion coefficient for the base material [61]. Thus, we do not distinguish them in this study. To allow the use of a fixed and uniform mesh throughout optimization, the ersatz material interpolation [64] is used in this work for an efficient approximation of elements that are cut by the level set boundary, as they have been demonstrated to be effective [43,65,66]. As the elemental Young's modulus is interpolated by the element area fraction, same  $\alpha_T$  is used for all the elements to avoid over penalization of thermal stress in the cut elements.

The design objective is to find the optimum microstructure for each subdomain such that resulting macrostructure has the minimum structural compliance induced by both mechanical and thermal loads with a specified amount of the base material. Thus, the optimization problem is formulated at the macroscale level with regard to the design variables at the microscale level

$$\underset{\Omega_{Y_{1}},\Omega_{Y_{2}},\dots,\Omega_{Y_{N}}}{\text{Minimize}} f\left(\Omega_{Y_{1}},\Omega_{Y_{2}},\dots,\Omega_{Y_{N}}\right) = \int_{\bigcup_{I=1}^{N}\Omega_{I}} \boldsymbol{b} \cdot \boldsymbol{u} \, d\Omega + \int_{\Gamma_{t}} \bar{\boldsymbol{t}} \cdot \boldsymbol{u} \, d\Gamma + \int_{\bigcup_{I=1}^{N}\Omega_{I}} \alpha_{T} \Delta T \, \boldsymbol{\varepsilon}^{0} : \mathbb{D}_{I}^{H} : \boldsymbol{\varepsilon}(\boldsymbol{u}) \, d\Omega$$
subject to  $a(\boldsymbol{u},\boldsymbol{v}) = \bar{a}(\Delta T,\boldsymbol{v}) + \ell(\boldsymbol{v}), \ \forall \boldsymbol{v} \in U_{ad}$ 

$$g_{I}(\Omega_{Y_{I}}) = \int_{\Omega_{Y_{I}}} d\Omega - V_{f_{I}} |Y_{I}| \leq 0, \ I = 1,2,\dots,N$$

$$(7)$$

where the objective f is defined as the total macrostructural compliance induced by mechanical and thermal loads,  $g_I$  is the volume fraction constraint for  $Y_I$  unit cell and  $V_{f_I}$  is the corresponding prescribed volume fraction constraint,  $|Y_I|$  is the volume of the unit cell  $Y_I$ .

## 3. Level set topology optimization method

In this study, Hadamard's boundary variation method is considered for shape optimization and the level set function is used to represent the boundary of a material microstructure implicitly,

$$\begin{cases}
\phi(x) \ge 0 & x \in \Omega_{Y} \\
\phi(x) = 0 & x \in \Gamma_{Y} \\
\phi(x) < 0 & x \in Y \setminus (\Omega_{Y} \cup \Gamma_{Y})
\end{cases} \tag{8}$$

where  $\phi(x)$  is the level set function at x in the unit cell Y,  $\Omega_Y$  is the material domain and  $\Gamma_Y$  is its boundary. The benefit of level set method is that a structure with smooth and well-defined boundary is always guaranteed, which is not easily attained by the traditional density-based methods. Thus, the optimized design can be directly additively manufactured without post-processing step so that the possible performance loss can be avoided. The following Hamilton-Jacobi equation [67–69] is solved to update the boundary described by  $\phi$ 

$$\frac{\partial \phi(x,t)}{\partial t} + V_n(x) |\nabla \phi(x,t)| = 0 \tag{9}$$

where  $V_n$  denotes the normal inward velocity of the structural boundary point x and t is the pseudo time. Eq. (9) can be written in a discrete form as

$$\phi_i^{k+1} = \phi_i^k - \Delta t |\nabla \phi_i^k| V_{n,i}$$
(10)

where k is the number of optimization iteration,  $\Delta t$  is the pseudo time step and  $V_{n,j}$  is the normal velocity at boundary point j. Here  $V_{n,j}$  are treated as the design variables updated by optimization. As a periodical re-initialization of  $\phi$  into the signed distance function is typically needed to regularize the level set function, in this study,  $\phi$  is reinitialized after every update in Eq. (10).

# 3.1. Multiscale optimization problem decomposition

Instead of solving the general optimization problem Eq. (7) directly, a variant of SLP method proposed by [70] is used, in which Eq. (7) are linearized about each material design  $\Omega_{Y_I}^k$  at current iteration k and then decomposed into N sub-problems [43] as follows

where  $\Delta\Omega_{Y_I}^k$  is the update for the current microscale design  $\Omega_{Y_I}^k$  within the bounds  $\Delta\Omega_{Y_I}$  and  $\Delta\Omega_{Y_I}$ , which are further determined by the Courant-Friedrichs-Lewy (CFL) stability condition as detailed later.  $\bar{g}_I^k$  denotes the constraint function change at the  $k^{th}$  iteration. The decomposed sub-problem for each unit cell can be solved independently and simultaneously. It is therefore, straight forward to distribute the computation and take advantage of parallel computing [43].

The method proposed in [71] is reproduced herein to solve Eq. (11). For a specific unit cell, the material level set boundary is first discretized into nb points. The element area fractions are then computed and used to interpolate the equilibrium Eqns. (3) to (6) to obtain the displacement field u and effective elasticity tensor  $\mathbb{D}^H$ . The sub-problem in Eq. (11) can be further expressed in a discrete form as (subscript I and superscript k are dropped for simplicity)

$$\frac{\partial f}{\partial \Omega_{Y}} \cdot \Delta \Omega_{Y} \approx \sum_{j=1}^{nb} \Delta t(s_{f,j}l_{j}) V_{n,j} = \Delta t \, \mathbf{S}_{f} \cdot \mathbf{V}_{n}$$

$$\frac{\partial g}{\partial \Omega_{Y}} \cdot \Delta \Omega_{Y} \approx \sum_{j=1}^{nb} \Delta t(s_{g,j}l_{j}) V_{n,j} = \Delta t \, \mathbf{S}_{g} \cdot \mathbf{V}_{n}$$
(12)

where  $s_{f,j}$  and  $s_{g,j}$  are the objective and constraint function sensitivities on the boundary point j, respectively,  $l_j$  is the discrete boundary length for point j,  $S_f$  and  $S_g$  are vectors collecting all the sensitivity and discrete boundary length multiplication, and  $V_n$  is the vector containing the boundary point normal velocities  $V_{n,j}$ . By replacing  $\Delta t V_n^k$  with  $\beta^k (S_f^k + \lambda^k S_g^k) / \|S_f^k + \lambda^k S_g^k\|_2$  [70], the actual optimization problem to be solved at current iteration k can be expressed by

$$\min_{\beta^{k},\lambda^{k}} \Delta t \mathbf{S}_{f}^{k} \cdot \mathbf{V}_{n}^{k}(\beta^{k},\lambda^{k})$$
s.t.  $\Delta t \mathbf{S}_{g}^{k} \cdot \mathbf{V}_{n}^{k}(\beta^{k},\lambda^{k}) \leq -\bar{g}^{k}$ 

$$\mathbf{V}_{n,min}^{k} \leq \mathbf{V}_{n}^{k} \leq \mathbf{V}_{n,max}^{k}$$
(13)

where  $V_{n,min}^k$  and  $V_{n,max}^k$  are the minimum and maximum velocities derived from the CFL condition, respectively. The optimization problem Eq. (13) is solved by the sequential least square SQP (SLSQP) method and the optimized  $\beta^k$  and  $\lambda^k$  are substituted back to  $\Delta t V_n^k = \beta^k (S_f^k + \lambda^k S_g^k) / ||S_f^k + \lambda^k S_g^k||_2$  to obtain the optimum  $\Delta t V_n^k$  at iteration k.  $\Delta t V_n^k$  is finally substituted back into Eq. (10) to update the level set function. For all examples in this paper, all boundary point movements at each iteration are limited to a half of a level set grid size.

### 3.2. Sensitivity analysis

The shape sensitivities of the objective f and constraint function  $g_I$  are needed to solve the decomposed sub-problems in Eq. (13). Ignoring the body forces in our problem, the compliance objective sensitivity can be derived as

$$f'(\Omega_{Y_I}) = -\int_{\Omega \in \Omega_I} \left( D_{I,ijkl}^{H'} \varepsilon_{ij}(\boldsymbol{u}) \varepsilon_{kl}(\boldsymbol{u}) - 2\alpha_T \Delta T D_{I,ijkl}^{H'} \varepsilon_{ij}^0 \varepsilon_{kl}(\boldsymbol{u}) \right) d\Omega$$
 (14)

where according to Eqs. (5) and (6), the shape sensitivity of  $D_{l,ijkl}^H$  can be written as

$$D_{I,ijkl}^{H'}(\Omega_{Y_I}) = \frac{1}{|Y_I|} \int_{\Gamma_{Y_I}} D_{pqrs} \left(\bar{\varepsilon}_{pq}^{(ij)} - \varepsilon_{pq}^{*(ij)}\right) \left(\bar{\varepsilon}_{rs}^{(kl)} - \varepsilon_{rs}^{*(kl)}\right) V_n d\Gamma$$
(15)

The shape sensitivity for the volume fraction constraint can be easily written as

$$g_I'(\Omega_{Y_I}) = \int_{\Gamma_{Y_I}} V_n d\Gamma \tag{16}$$

After calculating the sensitivities at Gauss points, the least square method is used to interpolate the sensitivities  $S_f$  and  $S_g$  at a boundary point [71].

### 4. Numerical examples

Several numerical examples are presented in this section to design material microstructures for a macrostructure under both mechanical and thermal loads. For the sake of simplicity, all involved quantities are dimensionless and normalized, and same mesh is used for the level set function and finite element analysis. The design domains of all the macrostructures and microstructures are discretized by 4-node quadrilateral bilinear elements with size  $1\times1$ , and the square unit cell with a  $100\times100$  FE mesh is used for all the material microstructure design domains. It is assumed that the isotropic base material has Young's modulus E=1, Poisson's ratio v=0.3 and thermal expansion coefficient  $\alpha_T=0.001$ . The void elements are assigned a weak Young's modulus of  $E=10^{-6}$ . The least square interpolation radius is set as 2. The optimization is terminated if the relative difference of objective function values between two successive steps is less than  $10^{-4}$ .

### 4.1. Material design for a cantilever beam

The first example is to design material microstructures for a cantilever beam as shown in Figure 2(a). The beam is fixed on the left edge and a downward load F = 1 is applied at the center of the right edge. The design domain experiences a uniform temperature change  $\Delta T$  and the allowable volume fraction of the solid phase for the microstructure is set to be 40% of the total unit cell volume. Figure 2(b) shows the initial design used for the microstructure domain.

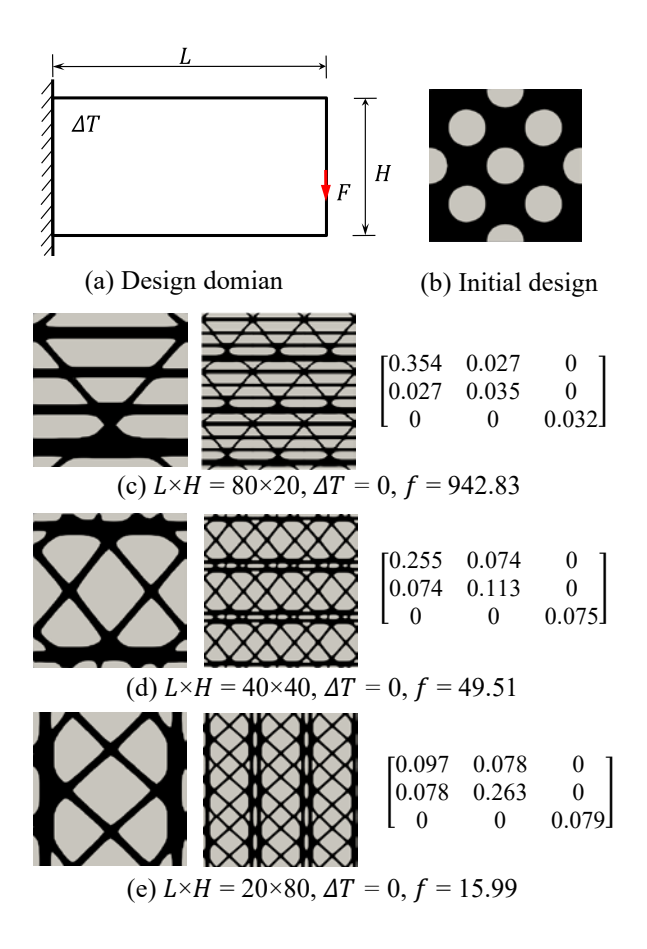


Figure 2. Optimized material microstructures for the cantilever beam with different  $L \times H$  under  $\Delta T = 0$  (left: unit cell; middle:  $3 \times 3$  array; right: effective elasticity matrix).

The optimized material designs with  $\Delta T = 0$  and various  $L \times H$  are firstly generated as shown in Figure 2(c)-(e), together with their optimized effective elasticity matrices. One can clearly see from Figure 2 that the macrostructural geometry has a big impact on the optimized material microstructure. When a long cantilever beam ( $L \times H = 80 \times 20$ ) is considered, material is designed with a larger stiffness in the horizontal direction to improve the bending resistance, as shown in Figure 2(c). As the beam gets shorter, the material stiffness in the vertical direction gradually increases to resist shearing, as indicated in Figure 2(d) and (e). It is worth noting that the designs of material microstructure with  $\Delta T = 0$  are all orthotropic even though no orthotropy constraint is enforced.

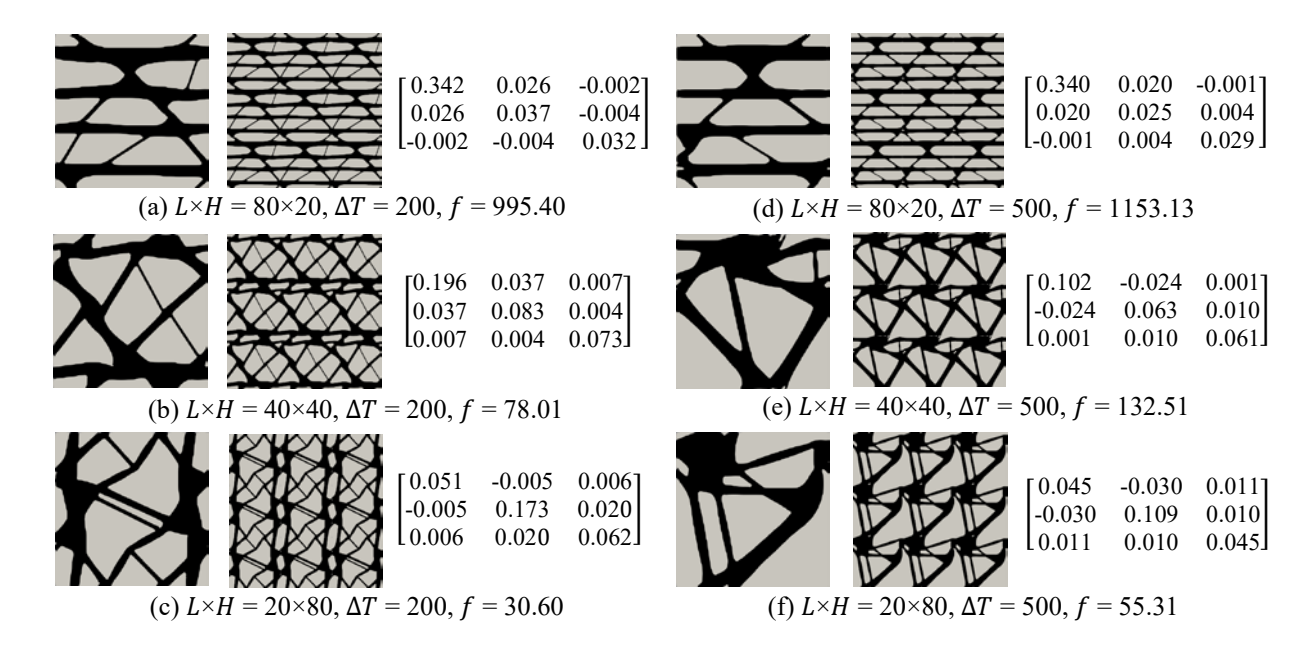


Figure 3. Optimized material microstructures for the cantilever beam with various  $L \times H$  under  $\Delta T = 200$  and  $\Delta T = 500$  (left: unit cell; middle:  $3 \times 3$  array; right: effective elasticity matrix).

Next, material designs with the same problem setting but non-zero temperature change  $\Delta T = 200$  and  $\Delta T = 500$  are generated in Figure 3 in which distinct differences in the designs can be observed when compared to the results with  $\Delta T = 0$  in Figure 2. The effective elasticity matrices indicate that the optimized material designs become anisotropic with an increasing  $\Delta T$  and anisotropic material can lead to a more minimum macrostructural compliance in the presence of the thermal load. The material designs also reduce  $D_{11}^H$ ,  $D_{12}^H$ ,  $D_{21}^H$  and  $D_{22}^H$  values with an increasing  $\Delta T$ . An examination of Eq. (4) reveals that these four components are directly related to the thermal expansion compliance therefore, reducing  $D_{11}^H$ ,  $D_{12}^H$ ,  $D_{21}^H$  and  $D_{22}^H$  minimizes the thermal compliance component. The  $D_{12}^H$  and  $D_{21}^H$  values become even negative when  $\Delta T = 500$  (see Figure 3(e) and (f)). Figure 4 depicts the iterative histories of the objective and constraint functions for obtaining the design in Figure 3(b), along with the intermediate designs at various iterations. It is observed that the structural compliance decreases rapidly during the first 100 iterations, due to

the increasing porosity of the material design which reduces the thermal expansion compliance. As the porosity increases, the mechanical load resistance of the design is weakened. The compliance then increases until the volume fraction constraint becomes feasible at around iteration 200. After that, the optimization converges smoothly to an optimized design that has a balanced resistance between the mechanical and thermal loads.

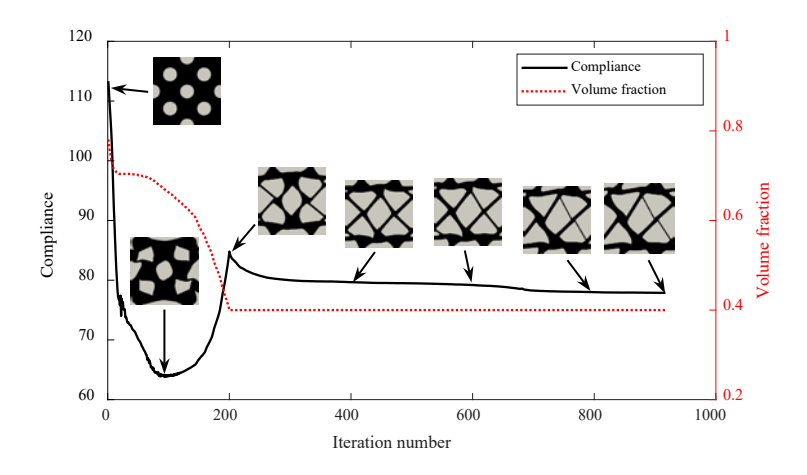


Figure 4. Convergence history of the objective function and volume fraction constraint for cantilever beam with  $L \times H = 40 \times 40$ ,  $\Delta T = 200$ .

It is noted that the thermal loads are less influential in the long cantilever beam  $L \times H = 80 \times 20$  even when  $\Delta T$  is high comparing the designs in Figure 3(a) and (d) to Figure 2(c). This is because for the long beam, a small decrease in the material stiffness in horizontal direction substantially reduces the beam bending resistance, resulting in a large increase in the mechanical component of the compliance. In other words, the mechanical load is the dominant influence on the final design over the thermal load in the long beam. As the beam gets shorter, the compliance contribution from the mechanical load decreases and that the thermal contribution becomes more influential in Figure 3(b), (c), (e) and (f). These results demonstrate that the geometry of the macrostructural design has a fundamental impact on the material design with non-zero thermal loads.

The proposed approach can design multiple material subdomains at different locations of the macrostructure and with different volume fraction constraints. To demonstrate this, a cantilever beam with  $L \times H = 80 \times 50$  and 4 subdomains is considered as shown in Figure 5(a), in which  $H_1 = H_4 = 10$  and  $H_2 = H_3 = 15$ . The volume fraction constraints are set as 0.5 for  $\Omega_2$  and  $\Omega_3$ , and 1 for  $\Omega_1$  and  $\Omega_4$ , i.e. no volume constraint is enforced for the top and bottom subdomains.

The optimized microstructures with  $\Delta T = 0$  and  $\Delta T = 500$  are shown in Figure 5(b) and (c), respectively, along with the design details given in Table I. One can see from Figure 5(b) that the optimized material designs are orthotropic and symmetric about the central horizontal axis when  $\Delta T = 0$ . However, the orthotropy and symmetry are broken down when the thermal load is non-zero, i.e.  $\Delta T = 500$ , in Figure 5(c). This is due to the fact that the thermal expansion load is a pressure dependent load. The material designs would be different in the tensile region of the top half of the beam from the compressive region in the bottom half.

One can see that although the allowable material for the top and bottom subdomains are 100%, porous material designs are suggested for these two regions when  $\Delta T = 500$ . This is because the fully solid material can produce large thermal expansion compliance compared to the porous material. Thus, instead of using up all the allowable material, it is better to have a porous design in the presence of the non-zero thermal loads. To illustrate the results, Figure 5(b) and (c) array  $16\times10$  optimized material unit cells. It should be noted that due to the assumption of length scale separation in the homogenization method, the optimum unit cell sizes should be infinitely small. Thus, the selection of unit cell sizes can affect the final material design and its performance. Typically, the more number of unit cells are considered, the better performance will be obtained. When the unit cell sizes are sufficiently small, the optimized design and its performance would not change significantly. This has been demonstrated in [52].

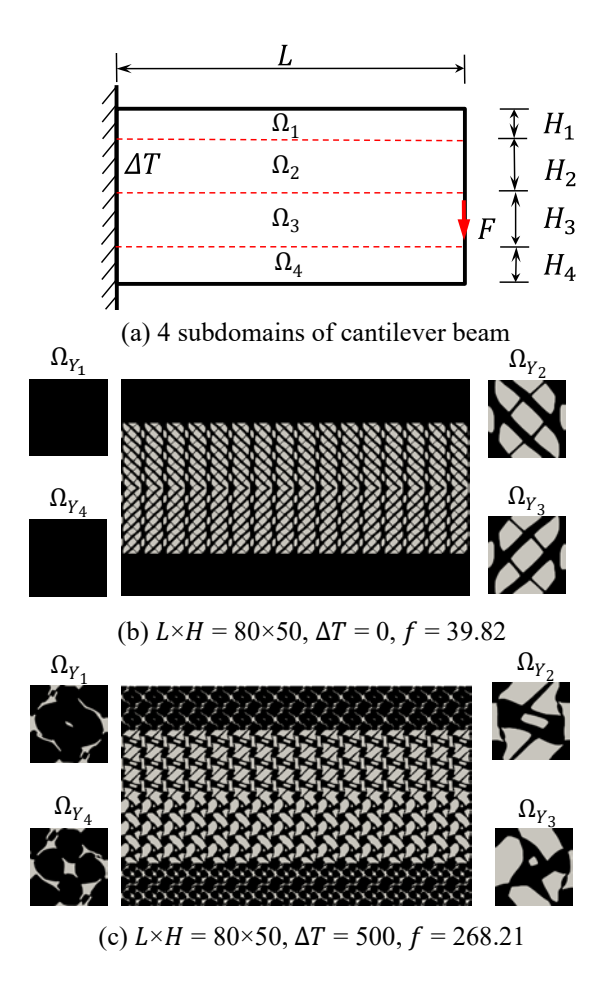


Figure 5. Optimized material microstructures for the cantilever beam with 4 material subdomains and different  $\Delta T$ .

Table I. Elasticity matrix and volume fraction of the microstructure designs in Figure 5.

Material subdomain	Figure 5(b)		Figure 5(c)		
	Effective elasticity matrix	Volume fraction	Effective elasticity matrix	Volume fraction	
$\Omega_{ m Y_1}$	$\begin{bmatrix} 1.099 & 0.330 & 0 \\ 0.330 & 1.099 & 0 \\ 0 & 0 & 0.385 \end{bmatrix}$	1	0.274     -0.073     0.013       -0.073     0.116     -0.002       0.013     0.002     0.126	0.910	
$\Omega_{ m Y_2}$	$\begin{bmatrix} 0.140 & 0.114 & 0 \\ 0.114 & 0.278 & 0 \\ 0 & 0 & 0.115 \end{bmatrix}$	0.5	$\begin{bmatrix} 0.042 & -0.028 & -0.023 \\ -0.028 & 0.080 & 0 \\ -0.023 & 0 & 0.068 \end{bmatrix}$	0.5	
$\Omega_{\mathrm{Y}_3}$	$\begin{bmatrix} 0.140 & 0.114 & 0 \\ 0.114 & 0.278 & 0 \\ 0 & 0 & 0.115 \end{bmatrix}$	0.5	$\begin{bmatrix} 0.036 & -0.021 & 0.019 \\ -0.021 & 0.066 & 0.014 \\ 0.019 & 0.014 & 0.083 \end{bmatrix}$	0.5	

$\Omega_{Y_4}$ $\begin{bmatrix} 1.0 \\ 0.3 \\ 0 \end{bmatrix}$	99 0.330 30 1.099 0	0 0 0.385	1	0.293 -0.064 0.029	-0.064 0.088 -0.003	0.029 -0.003 0.110	0.865
--	---------------------------	-----------------	---	--------------------------	---------------------------	--------------------------	-------

Additional parametric study is carried out to examine the influence of the number of material subdomains and the temperature change on the optimized macrostructural objective function. To this end, a  $L \times H = 80 \times 60$  cantilever beam composed of uniformly sized subdomains are considered, i.e.  $H_1 = H_2 = ... = H_{nr}$  in Figure 5(a) where nr indicates the number of subdomains. The results are shown in Table II, which reveal that when the number of subdomain is set to 1, an increase of  $\Delta T$  leads to a design with a greater compliance due to the increasing thermal compliance associated with the increasing temperature. When  $\Delta T = 500$ , an increase in nr leads to a lower compliance. This is due to the fact that when a larger number of subdomains is considered in the optimization, a larger design space is explored by the optimizer hence, an improved design performance can be expected.

Table II. Macrostructural compliance comparison with the optimized material microstructures with varying number of material subdomains and  $\Delta T$ ,  $L \times H = 80 \times 60$ .

1	nr = 1	$\Delta T = 500$		
$\Delta T$	Compliance	nr	Compliance	
0	81.88	1	282.26	
100	105.32	2	264.49	
200	152.75	3	246.42	
300	196.04	4	235.88	
400	244.16	5	227.03	
500	282.26	6	221.34	

## 4.2. Material design for a simply supported beam

The second example is the material design for a simply supported beam in Figure 6. The beam is subjected to  $\Delta T$  and 3 downward loads are applied on the top surface of the beam. The allowable

volume fraction of the solid phase for the material microstructure is set to be 40% of the total unit cell volume. The initial design for the microstructure is the same as the one shown in Figure 2(b).

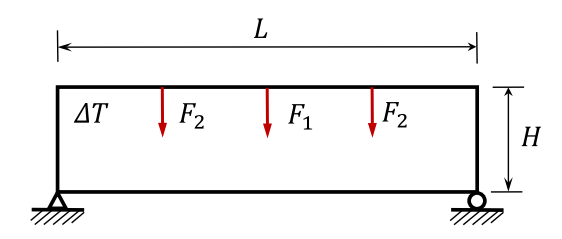


Figure 6. Simply supported beam with length L and height H.

The designs of the microstructures for the simply supported beam under a single loading case, i.e.,  $F_1 = 1$  and  $F_2 = 0$ , are firstly generated, and the resulting topologies with a range of  $\Delta T$  and various  $L \times H$  are given in Figure 7 along with the corresponding effective elasticity matrices. One can see from comparing Figure 7(a) and (d) versus Figure 2(c) and Figure 3(d) that even when the macrostructure geometries and  $\Delta T$  are the same, the macrostructural boundary condition has a significant influence on the optimized material design. Once again, orthotropic material designs are optimum for the simply supported beam when  $\Delta T = 0$ , while anisotropic microstructures with lower  $D_{11}^H$ ,  $D_{12}^H$ ,  $D_{21}^H$  and  $D_{22}^H$  values are found to be optimum when  $\Delta T = 500$ . The L/H ratio again affects the material designs for both  $\Delta T = 0$  and  $\Delta T = 500$  cases in terms of material horizontal and vertical stiffness. Therefore, the optimum macroscale and microscale designs are tightly coupled.

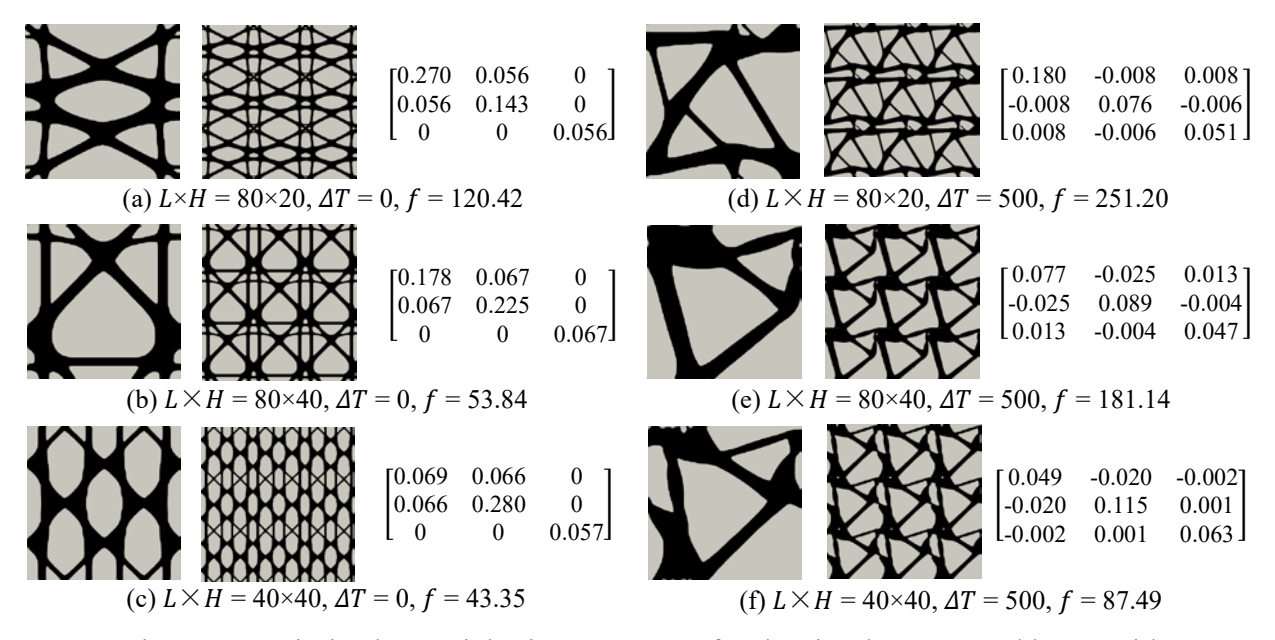


Figure 7. Optimized material microstructures for the simply supported beam with different  $L \times H$  under  $\Delta T = 0$  and  $\Delta T = 500$  (left: unit cell; middle:  $3 \times 3$  array; right: effective elasticity matrix).

Next, the simply supported beam under 3 symmetric loadings (i.e.,  $F_1 = F_2 = 1$ ) is optimized and their results are presented in Figure 8. Comparing Figure 7 to Figure 8, it is seen that for both  $\Delta T = 0$  and  $\Delta T = 500$  cases, the material microstructures with 3 loadings are generally different from those with 1 loading, and have higher stiffness in both horizontal ( $D_{11}$ ) and vertical directions ( $D_{22}$ ). It is interesting to notice from the right half of Figure 8 that even with non-zero temperature change  $\Delta T = 500$ , the optimized materials are completely or nearly orthotropic with 3 symmetric loadings, which is usually anisotropic with 1 loading. This example demonstrates that the loading cases of the macrostructure could also affect the anisotropy of the optimized material design even if  $\Delta T$  is non-zero.

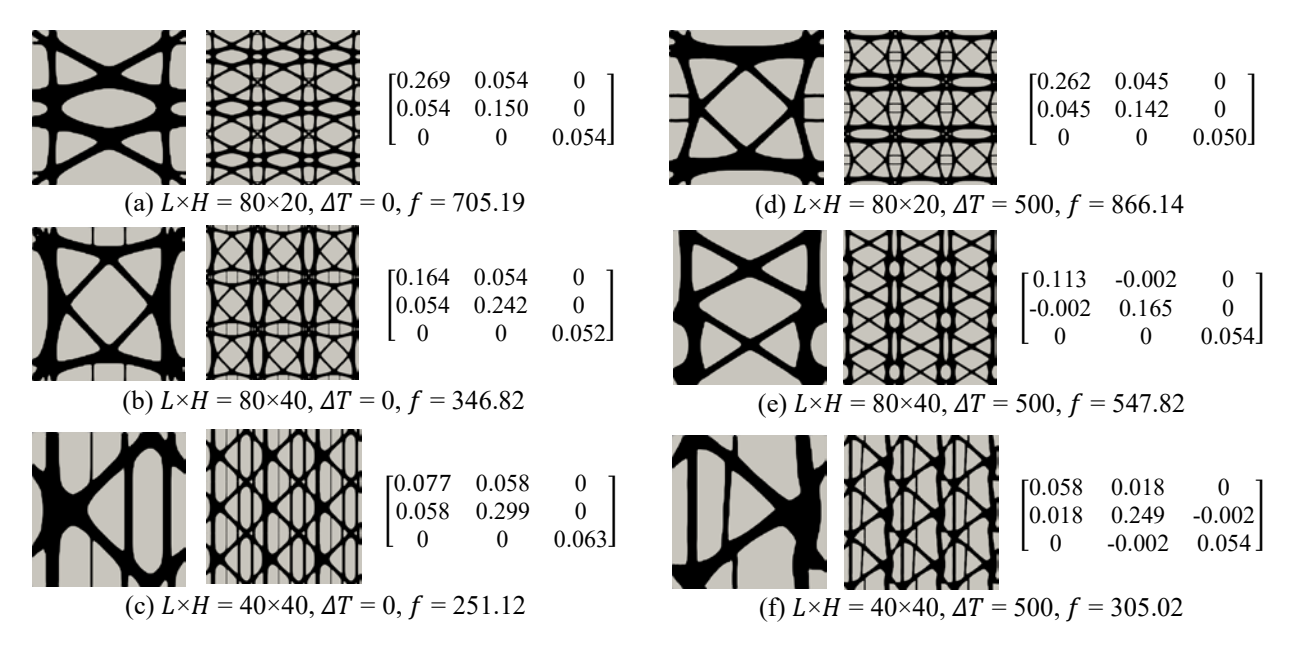


Figure 8. Optimized material microstructures for the 3 loadings simply supported beam with different  $L \times H$  under  $\Delta T = 0$  and  $\Delta T = 500$  (left: unit cell; middle:  $3 \times 3$  array; right: effective elasticity matrix).

#### 5. Conclusions

This paper introduces a level set topology optimization method to directly design architected material microstructures tailored for a macrostructure under both mechanical and thermal loads, based on the idea of multiscale topology optimization. The design variables are defined at the material scale and updated by optimizing the objective function formulated at the structural macroscale. The homogenization method is used to calculate the effective elastic matrix that bridges these two scales and the inverse homogenization method is used to determine the optimum microstructures. The numerical results demonstrate the effectiveness of the method and show that the optimized material designs for a thermoelastic macrostructure highly depends on the geometry, temperature change, mechanical loading and boundary conditions of the macroscopic structural design. In addition, the thermal loads can significantly influence the optimized material design in terms of material orthotropy, symmetry and porosity. When an increasing number of the material

subdomains is considered, a better overall performing and improved material designs is obtained. By incorporating the actual properties of AM base materials (e.g. thermoplastics, metals, alloys) and choosing the reasonable unit cell sizes, the proposed method can generate optimized architected material that is ready for AM. The current work can be naturally extended to simultaneously design macrostructural geometry and microscale material for thermoelasticity, which will be investigated in our future works.

### **Acknowledgments**

The presented work is supported by the NASA Transformational Tools and Technologies Project (Contract number NNX15AU22A) and DARPA (Award number HR0011-16-2-0032).

#### References

- 1. N. A. Fleck, V. S. Deshpande, and M. F. Ashby, in *Proc. R. Soc. A Math. Phys. Eng. Sci.* (2010), pp. 2495–2516.
- 2. L. J. Gibson and M. F. Ashby, *Cellular Solids: Structure and Properties* (Cambridge University Press, 1999).
- 3. X. Zheng, H. Lee, T. H. Weisgraber, M. Shusteff, J. DeOtte, E. B. Duoss, J. D. Kuntz, M. M. Biener, Q. Ge, J. A. Jackson, S. O. Kucheyev, N. X. Fang, and C. M. Spadaccini, Science (80-.). **344**, 1373 (2014).
- 4. T. A. Schaedler, A. J. Jacobsen, A. Torrents, A. E. Sorensen, J. Lian, J. R. Greer, L. Valdevit, and W. B. Carter, Science (80-.). **334**, 962 (2011).
- 5. N. Guo and M. C. Leu, Front. Mech. Eng. **8**, 215 (2013).
- 6. Q. Xu, Y. Lv, C. Dong, T. S. Sreeprased, A. Tian, H. Zhang, Y. Tang, Z. Yu, and N. Li, Nanoscale 7, 10883 (2015).
- 7. O. Sigmund, Int. J. Solids Struct. **31**, 2313 (1994).
- 8. X. Huang, A. Radman, and Y. M. Xie, Comput. Mater. Sci. **50**, 1861 (2011).
- 9. M. M. Neves, H. Rodrigues, and J. M. Guedes, Comput. Struct. 76, 421 (2000).

- 10. O. Sigmund, J. Mech. Phys. Solids 48, 397 (2000).
- 11. L. V. Gibiansky and O. Sigmund, J. Mech. Phys. Solids 48, 461 (2000).
- 12. J. Gao, H. Li, L. Gao, and M. Xiao, Adv. Eng. Softw. 116, 89 (2018).
- 13. O. Sigmund and S. Torquato, J. Mech. Phys. Solids 45, 1037 (1997).
- 14. O. Sigmund and J. Sø. Jensen, in *Philos. Trans. R. Soc. A Math. Phys. Eng. Sci.* (2003), pp. 1001–1019.
- 15. R. Alberdi and K. Khandelwal, Struct. Multidiscip. Optim. **59**, 461 (2019).
- 16. X. Y. Yang, X. Huang, J. H. Rong, and Y. M. Xie, Comput. Mater. Sci. 67, 229 (2013).
- 17. Y. Wang, Z. Luo, N. Zhang, and Z. Kang, Comput. Mater. Sci. 87, 178 (2014).
- 18. O. Sigmund, Mech. Mater. 20, 351 (1995).
- 19. F. Wang, O. Sigmund, and J. S. Jensen, J. Mech. Phys. Solids **69**, 156 (2014).
- 20. S. Torquato, S. Hyun, and A. Donev, Phys. Rev. Lett. **89**, (2002).
- 21. J. K. Guest and J. H. Prévost, Int. J. Solids Struct. 43, 7028 (2006).
- 22. V. J. Challis, A. P. Roberts, and A. H. Wilkins, Int. J. Solids Struct. 45, 4130 (2008).
- 23. Y. M. Yi, S. H. Park, and S. K. Youn, Int. J. Solids Struct. 37, 4791 (2000).
- 24. M. Osanov and J. K. Guest, Annu. Rev. Mater. Res. 46, 211 (2016).
- 25. T. A. Schaedler and W. B. Carter, Annu. Rev. Mater. Res. 46, 187 (2016).
- 26. J. Liu, A. T. Gaynor, S. Chen, Z. Kang, K. Suresh, A. Takezawa, L. Li, J. Kato, J. Tang, C. C. L. Wang, L. Cheng, X. Liang, and A. C. To, Struct. Multidiscip. Optim. 57, 2457 (2018).
- 27. O. Sigmund, S. Torquato, and I. A. Aksay, J. Mater. Res. 13, 1038 (1998).
- 28. S. J. Hollister, Nat. Mater. 4, 518 (2005).
- 29. J. Schwerdtfeger, F. Wein, G. Leugering, R. F. Singer, C. Körner, M. Stingl, and F. Schury, Adv. Mater. 23, 2650 (2011).
- 30. E. Andreassen, B. S. Lazarov, and O. Sigmund, Mech. Mater. 69, 1 (2014).
- 31. A. Clausen, F. Wang, J. S. Jensen, O. Sigmund, and J. A. Lewis, Adv. Mater. **27**, 5523 (2015).
- 32. A. Takezawa, M. Kobashi, and M. Kitamura, APL Mater. 3, (2015).

- 33. A. Takezawa and M. Kobashi, Compos. Part B Eng. 131, 21 (2017).
- 34. D. Xiao, Y. Yang, X. Su, D. Wang, and J. Sun, Biomed. Mater. Eng. 23, 433 (2013).
- 35. C. Y. Lin, T. Wirtz, F. LaMarca, and S. J. Hollister, J. Biomed. Mater. Res. Part A 83, 272 (2007).
- 36. Y. Koizumi, A. Okazaki, A. Chiba, T. Kato, and A. Takezawa, Addit. Manuf. 12, 305 (2016).
- 37. X. Huang, S. W. Zhou, Y. M. Xie, and Q. Li, Comput. Mater. Sci. 67, 397 (2013).
- 38. H. Rodrigues, J. M. Guedes, and M. P. Bendsoe, Struct. Multidiscip. Optim. 24, 1 (2002).
- 39. P. G. Coelho, P. R. Fernandes, J. M. Guedes, and H. C. Rodrigues, Struct. Multidiscip. Optim. **35**, 107 (2008).
- 40. L. Liu, J. Yan, and G. Cheng, Comput. Struct. **86**, 1417 (2008).
- 41. L. Xia and P. Breitkopf, Comput. Methods Appl. Mech. Eng. 278, 524 (2014).
- 42. W. M. Vicente, Z. H. Zuo, R. Pavanello, T. K. L. Calixto, R. Picelli, and Y. M. Xie, Comput. Methods Appl. Mech. Eng. **301**, 116 (2016).
- 43. R. Sivapuram, P. D. Dunning, and H. A. Kim, Struct. Multidiscip. Optim. 54, 1267 (2016).
- 44. Y. Zhang, H. Li, M. Xiao, L. Gao, S. Chu, and J. Zhang, Struct. Multidiscip. Optim. 59, 1273 (2019).
- 45. Y. Zhang, M. Xiao, L. Gao, J. Gao, and H. Li, Mech. Syst. Signal Process. **135**, 106369 (2020).
- 46. A. Abdulle and A. Di Blasio, Multiscale Model. Simul. 17, 399 (2019).
- 47. Perle Geoffroy Donders, Homogenization Method for Topology Optmization of Struc-Tures Built with Lattice Materials, Ecole Polytechnique, 2018.
- 48. C. Barbarosie and A. M. Toader, Mech. Adv. Mater. Struct. 19, 290 (2012).
- 49. R. Lipton and M. Stuebner, Struct. Multidiscip. Optim. 33, 351 (2007).
- 50. G. Allaire, P. Geoffroy-Donders, and O. Pantz, Comput. Math. with Appl. 78, 2197 (2019).
- 51. A. Faure, G. Michailidis, R. Estevez, G. Parry, and G. Allaire, in *ECCOMAS Congr. 2016 Proc. 7th Eur. Congr. Comput. Methods Appl. Sci. Eng.*, edited by V. P. M. Papadrakakis, V. Papadopoulos, G. Stefanou (Crete Island, Greece, 2016), pp. 3534–3545.
- 52. Z. H. Zuo, X. Huang, J. H. Rong, and Y. M. Xie, Mater. Des. 51, 1023 (2013).

- 53. F. Fritzen, L. Xia, M. Leuschner, and P. Breitkopf, Int. J. Numer. Methods Eng. **106**, 430 (2016).
- 54. J. Kato, D. Yachi, T. Kyoya, and K. Terada, Int. J. Numer. Methods Eng. 113, 1189 (2018).
- 55. P. B. Nakshatrala, D. A. Tortorelli, and K. B. Nakshatrala, Comput. Methods Appl. Mech. Eng. **261–262**, 167 (2013).
- 56. H. Rodrigues and P. Fernandes, Int. J. Numer. Methods Eng. 38, 1951 (1995).
- 57. T. Gao and W. Zhang, Struct. Multidiscip. Optim. 42, 725 (2010).
- 58. Q. Li, G. P. Steven, and Y. M. Xie, J. Therm. Stress. **24**, 347 (2001).
- 59. P. Pedersen and N. L. Pedersen, Struct. Multidiscip. Optim. 42, 681 (2010).
- 60. Q. Xia and M. Y. Wang, Comput. Mech. 42, 837 (2008).
- 61. J. Deng, J. Yan, and G. Cheng, Struct. Multidiscip. Optim. 47, 583 (2013).
- 62. J. Yan, X. Guo, and G. Cheng, Comput. Mech. 57, 437 (2016).
- 63. J. Guedes and N. Kikuchi, Comput. Methods Appl. Mech. Eng. 83, 143 (1990).
- 64. P. D. Dunning, H. A. Kim, and G. Mullineux, Finite Elem. Anal. Des. 47, 933 (2011).
- 65. H. Chung, O. Amir, and H. A. Kim, Comput. Methods Appl. Mech. Eng. Accepted, (2019).
- 66. S. Kambampati, R. Picelli, and H. A. Kim, in *AIAA Scitech 2019 Forum* (American Institute of Aeronautics and Astronautics, Reston, Virginia, 2019).
- 67. J. A. Sethian and A. Wiegmann, J. Comput. Phys. 163, 489 (2000).
- 68. Y. Mei and X. Wang, Acta Mech. Sin. Xuebao 20, 507 (2004).
- 69. G. Allaire, F. Jouve, and A. M. Toader, J. Comput. Phys. 194, 363 (2004).
- 70. P. D. Dunning and H. A. Kim, Struct. Multidiscip. Optim. 51, 631 (2015).
- 71. R. Picelli, S. Townsend, C. Brampton, J. Norato, and H. A. Kim, Comput. Methods Appl. Mech. Eng. **329**, 1 (2018).